MIT Open Access Articles

Measurement of the Two-Neutrino Double-Beta Decay Half-Life of ^{130}Te with the CUORE-0 Experiment

Massachusetts Institute of Technology

Measurement of the two-neutrino double-beta decay half-life of ^{130}Te with the CUORE-0 experiment

C. Alduino[1], K. Alfonso[2], D. R. Artusa[1,3], F. T. Avignone III[1], O. Azzolini[4], T. I. Banks[5,6], G. Bari[7], J. W. Beeman[8], F. Bellini[9,10], A. Bersani[11], M. Biassoni[13], C. Brofferio[12,13], C. Bucci[3], A. Camacho[4], A. Caminata[11], L. Canonica[3,22], X. G. Cao[14], S. Capelli[12,13], L. Cappelli[3], L. Carbone[13], L. Cardani[9,10], P. Carniti[12,13], N. Casali[9,10], L. Cassina[12,13], D. Chiesa[12,13], N. Chott[1], M. Clemenza[12,13], S. Copello[11,16], C. Cosmelli[9,10], O. Cremonesi[13,a], R. J. Creswick[1], J. S. Cushman[17], A. D'Addabbo[3], I. Dafinei[10], C. J. Davis[17], S. Dell'Oro[3,18], M. M. Deninno[7], S. Di Domizio[11,16], M. L. Di Vacri[3], A. Drobizhev[5,6], D. Q. Fang[14], M. Faverzani[12,13], J. Feintzeig[6], G. Fernandes[11,16], E. Ferri[13], F. Ferroni[9,10], E. Fiorini[12,13], M. A. Franceschi[20], S. J. Freedman[5,6,b], B. K. Fujikawa[6], A. Giachero[13], L. Gironi[12,13], A. Giuliani[21], L. Gladstone[22], P. Gorla[3], C. Gotti[12,13], T. D. Gutierrez[23], E. E. Haller[8,24], K. Han[17,25], E. Hansen[2,22], K. M. Heeger[17], R. Hennings-Yeomans[5,6], K. P. Hickerson[2], H. Z. Huang[2], R. Kadel[26], G. Keppel[4], Yu. G. Kolomensky[5,6,26], A. Leder[22], C. Ligi[20], K. E. Lim[17], X. Liu[2], Y. G. Ma[14], M. Maino[12,13], L. Marini[11,16], M. Martinez[9,10,27], R. H. Maruyama[17], Y. Mei[6], N. Moggi[7,28], S. Morganti[10], P. J. Mosteiro[10], T. Napolitano[20], C. Nones[29], E. B. Norman[30,31], A. Nucciotti[12,13], T. O'Donnell[5,6], F. Orio[10], J. L. Ouellet[5,6,22], C. E. Pagliarone[3,15], M. Pallavicini[11,16], V. Palmieri[4], L. Pattavina[3], M. Pavan[12,13], G. Pessina[13], V. Pettinacci[10], G. Piperno[20], C. Pira[4], S. Pirro[3], S. Pozzi[12,13], E. Previtali[13], C. Rosenfeld[1], C. Rusconi[13], S. Sangiorgio[30], D. Santone[3,19], N. D. Scielzo[30], V. Singh[5], M. Sisti[12,13], A. R. Smith[6], L. Taffarello[32], M. Tenconi[21], F. Terranova[12,13], C. Tomei[10], S. Trentalange[2], M. Vignati[10], S. L. Wagaarachchi[5,6], B. S. Wang[30,31], H. W. Wang[14], J. Wilson[1], L. A. Winslow[22], T. Wise[17,33], A. Woodcraft[34], L. Zanotti[12,13], G. Q. Zhang[14], B. X. Zhu[2], S. Zimmermann[35], S. Zucchelli[7,36]

[1] Department of Physics and Astronomy, University of South Carolina, Columbia, SC 29208, USA
[2] Department of Physics and Astronomy, University of California, Los Angeles, CA 90095, USA
[3] INFN-Laboratori Nazionali del Gran Sasso, 67010 Assergi, L'Aquila, Italy
[4] INFN-Laboratori Nazionali di Legnaro, 35020 Legnaro, Padova, Italy
[5] Department of Physics, University of California, Berkeley, CA 94720, USA
[6] Nuclear Science Division, Lawrence Berkeley National Laboratory, Berkeley, CA 94720, USA
[7] INFN-Sezione di Bologna, 40127 Bologna, Italy
[8] Materials Science Division, Lawrence Berkeley National Laboratory, Berkeley, CA 94720, USA
[9] Dipartimento di Fisica, Sapienza Università di Roma, 00185 Rome, Italy
[10] INFN-Sezione di Roma, 00185 Rome, Italy
[11] INFN-Sezione di Genova, 16146 Genova, Italy
[12] Dipartimento di Fisica, Università di Milano-Bicocca, 20126 Milan, Italy
[13] INFN-Sezione di Milano Bicocca, 20126 Milan, Italy
[14] Shanghai Institute of Applied Physics, Chinese Academy of Sciences, Shanghai 201800, China
[15] Dipartimento di Ingegneria Civile e Meccanica, Università degli Studi di Cassino e del Lazio Meridionale, 03043 Cassino, Italy
[16] Dipartimento di Fisica, Università di Genova, 16146 Genova, Italy
[17] Department of Physics, Yale University, New Haven, CT 06520, USA
[18] INFN-Gran Sasso Science Institute, 67100 L'Aquila, Italy
[19] Dipartimento di Scienze Fisiche e Chimiche, Università dell'Aquila, 67100 L'Aquila, Italy
[20] INFN-Laboratori Nazionali di Frascati, 00044 Frascati, Rome, Italy
[21] CSNSM, Univ. Paris-Sud, CNRS/IN2P3, Université Paris-Saclay, 91405 Orsay, France
[22] Massachusetts Institute of Technology, Cambridge, MA 02139, USA
[23] Physics Department, California Polytechnic State University, San Luis Obispo, CA 93407, USA
[24] Department of Materials Science and Engineering, University of California, Berkeley, CA 94720, USA
[25] Department of Physics and Astronomy, Shanghai Jiao Tong University, Shanghai 200240, China
[26] Physics Division, Lawrence Berkeley National Laboratory, Berkeley, CA 94720, USA
[27] Laboratorio de Fisica Nuclear y Astroparticulas, Universidad de Zaragoza, 50009 Zaragoza, Spain
[28] Dipartimento di Scienze per la Qualità della Vita, Alma Mater Studiorum-Università di Bologna, 47921 Bologna, Italy
[29] Service de Physique des Particules, CEA/Saclay, 91191 Gif-sur-Yvette, France
[30] Lawrence Livermore National Laboratory, Livermore, CA 94550, USA
[31] Department of Nuclear Engineering, University of California, Berkeley, CA 94720, USA

[32] INFN-Sezione di Padova, Padova 35131, Italy

[33] Department of Physics, University of Wisconsin, Madison, WI 53706, USA

[34] SUPA, Institute for Astronomy, University of Edinburgh, Blackford Hill, Edinburgh EH9 3HJ, UK

[35] Engineering Division, Lawrence Berkeley National Laboratory, Berkeley, CA 94720, USA

[36] Dipartimento di Fisica e Astronomia, Alma Mater Studiorum-Università di Bologna, 40127 Bologna, Italy

Abstract We report on the measurement of the two-neutrino double-beta decay half-life of ^{130}Te with the CUORE-0 detector. From an exposure of 33.4 kg year of TeO$_2$, the half-life is determined to be $T_{1/2}^{2\nu} = [8.2 \pm 0.2$ (stat.) ± 0.6 (syst.)$] \times 10^{20}$ year. This result is obtained after a detailed reconstruction of the sources responsible for the CUORE-0 counting rate, with a specific study of those contributing to the ^{130}Te neutrinoless double-beta decay region of interest.

1 Introduction

Double-beta decay is a rare nuclear process in which two nucleons simultaneously decay and emit two electrons. The allowed Standard Model version of this process emits two (anti-)neutrinos and is called two-neutrino double-beta decay ($2\nu\beta\beta$). This decay is interesting in its own right as the slowest process ever directly observed [1,2]. Moreover, it may represent an important source of background for the neutrinoless double-beta decay ($0\nu\beta\beta$), i.e. a related process with no neutrino emission [3]. $0\nu\beta\beta$ manifestly violates lepton number and therefore its discovery would point to new physics beyond the Standard Model. Experiments searching for $0\nu\beta\beta$ have made great leaps forward in sensitivity by using a variety of techniques and isotopes [1,2,4,5].

The Cryogenic Underground Observatory for Rare Events (CUORE) [6,7] is the latest and most massive in a family of bolometric detectors designed to search for the $0\nu\beta\beta$ decay of ^{130}Te (Q-value = 2528 keV [8–10]). The detector combines the excellent energy resolution achievable with the bolometric technique ($\sim$5 keV at 2615 keV) with the exceptionally high natural abundance of ^{130}Te (34%). The first phase of CUORE, named CUORE-0, was 1/19th the size of CUORE and operated at the Laboratori Nazionali del Gran Sasso (LNGS), in Italy, between 2013 and 2015. In addition to being a competitive $0\nu\beta\beta$ experiment [5,11,12], CUORE-0 is a test of the assembly protocols for CUORE: the reconstruction of background sources responsible for the CUORE-0 counting rate enables us to verify that the necessary background requirements for CUORE are fulfilled.

In bolometers, the neutrinos emitted in $2\nu\beta\beta$ are not detected, and the summed kinetic energy of the two electrons forms a continuous spectrum from 0 keV up to the Q-value of the decay. Conversely, $0\nu\beta\beta$ produces no neutrinos and the experimental signature is a sharp peak at the Q-value of the decay, broadened by the energy resolution of the detector. This broadening smears $2\nu\beta\beta$ events into the $0\nu\beta\beta$ region of interest (ROI) around the Q-value and forms an irreducible background to the $0\nu\beta\beta$ signal; thus a good energy resolution is key to mitigating this background.

The other background contributions in the ROI come from naturally occurring radioactivity in the detector components. These background sources can be disentangled and described quantitatively by carefully analyzing the shape of the measured spectrum and constructing a detailed background model, including both physics processes and instrumental effects.

This paper reports the CUORE-0 background model as well as a new precision measurement of the ^{130}Te $2\nu\beta\beta$ half-life. We use a detailed Geant4-based simulation and a Bayesian fitting algorithm with a priori constraints from materials assay to reconstruct the experimental data and form a posteriori estimates of the background source activities. A frequentist analysis, using the same model, is presented in [13].

We present the experimental details, including the data acquisition and analysis chain, in Sect. 2. Background constraints from external measurements are summarized in Sect. 3. The construction of the Monte Carlo simulation code is presented in Sect. 4. The validation of Monte Carlo simulations, by comparing external radioactive source calibration spectra with the data, is presented in Sect. 5. The set of identified background sources and their effects on the experimental data is discussed in Sect. 6. The Bayesian fitting tool is introduced in Sect. 7. We present the fit results and discuss their uncertainties in Sect. 8. Finally, the $2\nu\beta\beta$ decay half-life evaluation is presented in Sect. 9 and the $0\nu\beta\beta$ ROI reconstruction is discussed in Sect. 10.

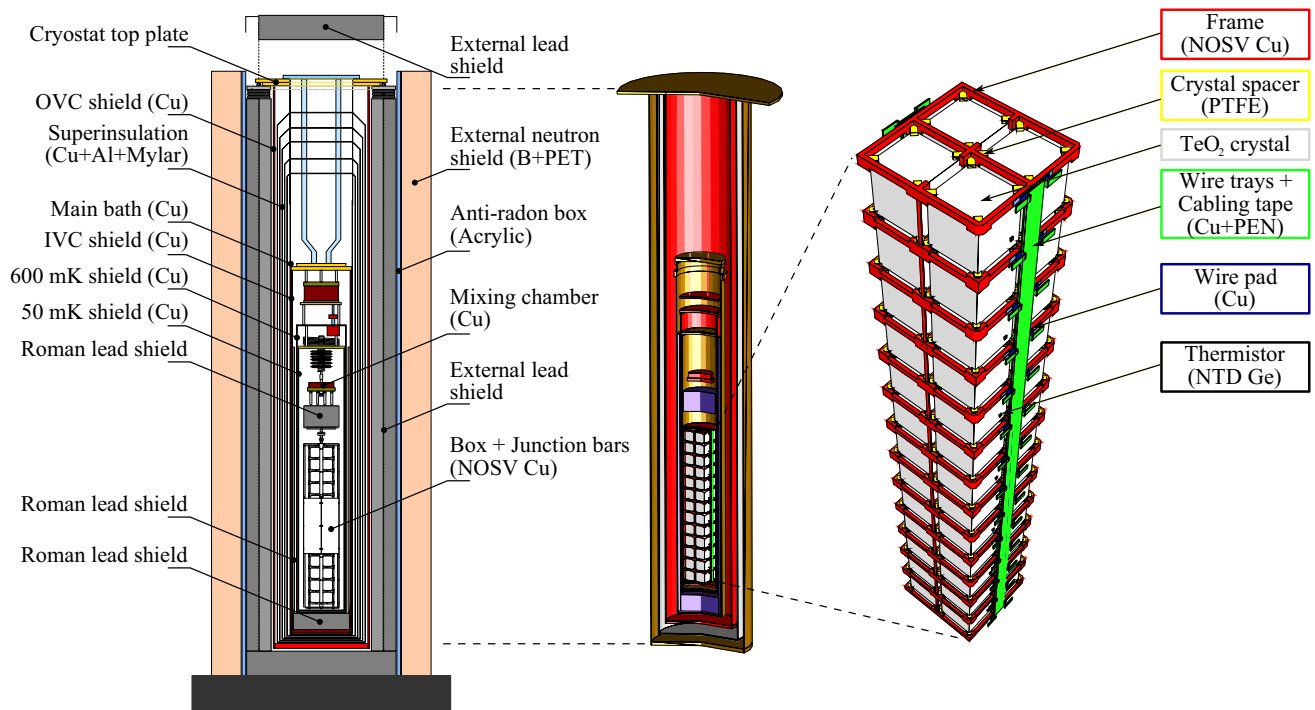[a] e-mail: cuore-spokesperson@lngs.infn.it

[b] Deceased

Fig. 1 The CUORE-0 as built (*left*) compared to the implementation in the simulation (*middle*). The details of the *tower structure* are shown as implemented in the simulation (*right*). Detector floors are numbered starting with floor 1 at the bottom

2 Experiment

The CUORE-0 detector is one tower of 52 $^{nat}TeO_2$ crystals arranged in 13 floors, each with 4 crystals [14]. Each crystal is 750 g and is operated as an independent bolometer at ~10 mK. At these temperatures, the interaction of a particle with the crystal generates a measurable temperature rise proportional to the energy deposited. The total detector mass is 39 kg of TeO_2, or 10.8 kg of ^{130}Te.

The tower is situated in a dilution refrigerator that provides the cooling power necessary to keep the TeO_2 crystals at their working temperature. The copper and PTFE support structure holds the crystals and provides the thermal link to the refrigerator. The tower is surrounded by several layers of shielding, including low-background Roman lead and an anti-radon box. A schematic of the experiment is shown in Fig. 1 (left). The crystals temperatures are measured continuously using neutron transmutation doped (NTD) germanium thermistors, coupled to the crystals using epoxy. The thermistors convert temperature variations to a voltage output, which is digitized at a rate of 125 Samples/s. A software trigger is used to identify events and collect them in 5 s windows. Each window is divided into two periods: 1 s before the trigger and 4 s after it. The period before the trigger is used to establish the baseline temperature of the crystal and the remaining 4 s is used to determine the pulse amplitude. Together these are used to extract the energy deposited.

A silicon resistor is also coupled to each crystal with epoxy and is used to generate reference thermal pulses every 300 s. These are used to stabilize the gain of the bolometer against temperature fluctuations. Forced triggers are used for noise and threshold studies. The threshold (in the default high-energy triggered data used for this analysis) is bolometer dependent and is approximately between 30 and 120 keV. The energy response is calibrated by inserting thoriated tungsten wires inside the outer vessel of the cryostat, and using the γ lines from the ^{232}Th decay chain to calibrate each bolometer independently.

The details of the CUORE-0 detector design, operation and performance are described in [14]. New protocols for material selection, cleaning, and handling were developed for the detector crystals and tower support structure. The dilution refrigerator, shielding, and other cryostat components are those from the Cuoricino experiment [15,16].

2.1 Data production

This analysis uses data collected with CUORE-0 from March 2013 to March 2015. The data are grouped in datasets, which last approximately one month. Each dataset has approximately three days of calibration data at both the beginning and the end, collected while the detector was exposed to a radioactive calibration source. In total, 20 datasets were used in the $0\nu\beta\beta$ analysis: however, in the present analysis we

exclude the first dataset because of a substantial (∼15 keV) miscalibration in the highest energy region (above 3 MeV). The physics data (i.e. excluding the calibration data of each dataset) use a total of 33.4 kg year of TeO_2 exposure, or 9.3 kg year of ^{130}Te exposure, after all data quality selections.

The data production converts the data from a series of triggered waveforms into a calibrated energy spectrum. The details of the data production can be found in [12], but we outline the general procedure here. The entire waveform is used to extract the amplitude of the pulse. Then each bolometer in each dataset is calibrated independently. A time-coincidence analysis is performed to search for events that deposit energy across multiple bolometers. Finally, the $0\nu\beta\beta$ ROI (2470–2580 keV) is blinded for analysis.

Once the data are blinded, we implement a series of event selection cuts to maximize our sensitivity to physics events. We exclude periods of cryostat instability and malfunction. We enforce a pile-up cut of 7.1 s around each event: the 3.1 s before and 4 s after the event. We apply a series of pulse shape cuts to reject deformed or non-physical events mostly contaminating the low-energy region below ∼400 keV.

Double-beta decay events are usually confined within the crystal they originated from. However, many background sources deposit energy in multiple crystals within the response time of the detector. We use this information in the analysis by forming multiplets of events that occur within a coincidence window of ±5 ms in different crystals. Since the event rate is approximately 1 mHz, the probability of accidental (i.e. causally unrelated) coincidences is extremely small (∼10^{-5}).

We then build energy spectra from these multiplets:

– $\mathcal{M}$ spectrum is the energy spectrum of all events, with no coincidence criteria applied;
– $\mathcal{M}_1$ spectrum is the energy spectrum of the events with the requirement that only one bolometer triggered (multiplicity 1 or $\mathcal{M}_1$ events);
– $\mathcal{M}_2$ spectrum is the energy spectrum of the events with the requirement that two bolometers triggered (multiplicity 2 or $\mathcal{M}_2$ events);
– Σ_2 spectrum is the energy spectrum associated to $\mathcal{M}_2$ multiplets, each multiplet produces an entry with an energy $E(\Sigma_2)$ that is the sum of the energies of the two events composing the multiplet.

Higher-order multiplets are used only to evaluate the contribution of muons to the background.

The signal cut efficiency as a function of energy is defined as the fraction of true signal events that pass all the event cuts. In [12], we calculated the efficiency of these cuts by measuring their effect on γ-peaks in the energy spectrum. This takes advantage of the fact that the events in the γ-peaks are a nearly pure sample of true signal events. In the present anal-

ysis we use a new technique, which takes advantage of the coincidence analysis and allows a better reproduction of the energy dependence of the efficiency. Since accidental coincidences are negligible, $\mathcal{M}_2$ events provide a pure sample of good events on the whole energy spectrum. The cut efficiency ε_C is modeled as an exponential function of the energy, $\varepsilon_C(1 - e^{-E/E_c})$, which is fitted to $\mathcal{M}_2$ events on a bin-by-bin basis; it rapidly reaches a stable value of $\varepsilon_C = 0.943 \pm 0.002$ at energies above $E_c \sim 100$ keV. This is consistent with the signal cut efficiency quoted in [12] of 0.937 ± 0.007. Above $E \sim 7$ MeV the $\mathcal{M}_2$ spectra have insufficient statistics to give meaningful fit results. Therefore, in this analysis we do not include events with energy above 7 MeV.

3 Background sources

In rare event searches, some backgrounds are ubiquitous due to the natural decay of ^{40}K and the daughters of the ^{232}Th and ^{238}U decay chains, including the surface implantation of ^{210}Pb from environmental ^{222}Rn. Based on the results of previous bolometric experiments [15–17], we expect these radioactive contaminants to be located in the whole experimental setup, including the detector itself. The cosmogenic activation, especially of copper and tellurium, resulting in ^{60}Co is also of concern. A small contribution from cosmic muons [18], environmental gamma rays (γ) [19], and neutrons interacting directly in the detector is expected [19]. With this in mind, extreme care was taken into the selection of the materials used to build the CUORE-0 detector [14], and in the cleaning of all surfaces facing each TeO_2 crystal [20,21]. A lot of effort was also devoted to the detector design, to minimize both the total mass of the inactive parts of the detector tower and the surface area facing the array; the detector assembly procedure under controlled atmosphere [14]; and the optimization of the production protocol of every detector component to limit exposure to cosmic rays.

Tables 1 and 2 report the bulk and surface activities from the screening of the CUORE-0 components. A discussion of the different assay techniques that we used to derive the quoted contamination limits can be found in [17,20]. The Cuoricino results (this experiment used the same cryostat and shield as CUORE-0) and screening results guide the construction of the background model and the definition of the priors on material contaminants.

4 Monte Carlo

The background sources are simulated using a Geant4-based Monte Carlo code called *MCuoreZ*. The code generates and propagates primary and any secondary particles through the CUORE-0 geometry until they are detected in the TeO_2 crystals. The code outputs the energy and time of the energy

Table 1 Measurements and limits on bulk contaminations of the various detector components, as obtained with different measurement techniques: bolometric, Neutron Activation Analysis, Inductively Coupled Plasma Mass Spectrometry, High Purity Ge γ spectroscopy. Error bars are 1 sigma, limits are 90% C.L. upper limits

Component	^{232}Th [Bq/kg]	^{238}U [Bq/kg]	^{40}K [Bq/kg]
TeO$_2$ crystals	$<8.4 \times 10^{-7}$	$<6.7 \times 10^{-7}$	
Epoxy	$<8.9 \times 10^{-4}$	$<1.0 \times 10^{-2}$	$<47 \times 10^{-3}$
Au bonding wires	$<4.1 \times 10^{-2}$	$<1.2 \times 10^{-2}$	
Si heaters	$<3.3 \times 10^{-4}$	$<2.1 \times 10^{-3}$	
Ge thermistors	$<4.1 \times 10^{-3}$	$<1.2 \times 10^{-2}$	
PEN-Cu cables	$<1.0 \times 10^{-3}$	$<1.3 \times 10^{-3}$	$<1.3 \times 10^{-2}$
PTFE supports	$<6.1 \times 10^{-6}$	$<2.2 \times 10^{-5}$	
Cu NOSV	$<2.0 \times 10^{-6}$	$<6.5 \times 10^{-5}$	$7 \pm 2 \times 10^{-4}$
Pb Roman	$<4.5 \times 10^{-5}$	$<4.6 \times 10^{-5}$	$<2.3 \times 10^{-5}$
Pb Ext	$<2.6 \times 10^{-4}$	$<7.0 \times 10^{-4}$	$<5.4 \times 10^{-3}$

Table 2 90% C.L. upper limits for the surface contaminants of the most relevant elements facing the CUORE-0 detector, as obtained with different measurement techniques: bolometric, Neutron Activation Analysis, and α spectroscopy with Si barrier detectors. Different contamination depths are considered: 0.01–10 μm for crystals; 0.1–10 μm for heaters, thermistors and CuNOSV; and 0.1–30 μm for PEN and PTFE components (contamination depths are further discussed in Sect. 6.2)

Component	^{232}Th [Bq/cm^2]	^{238}U [Bq/cm^2]	^{210}Pb [Bq/cm^2]
TeO$_2$ crystals [22]	$<2 \times 10^{-9}$	$<9 \times 10^{-9}$	$<1 \times 10^{-6}$
Si heaters [23,24]	$<3 \times 10^{-6}$	$<8 \times 10^{-7}$	$<8 \times 10^{-7}$
Ge thermistors	$<8 \times 10^{-6}$	$<5 \times 10^{-6}$	$<4 \times 10^{-5}$
PEN-Cu cables	$<4 \times 10^{-6}$	$<5 \times 10^{-6}$	$<3 \times 10^{-5}$
PTFE supports	$<2 \times 10^{-8}$	$<7 \times 10^{-8}$	
CuNOSV [20]	$<7 \times 10^{-8}$	$<7 \times 10^{-8}$	$<9 \times 10^{-7}$

depositions (time is used to properly take into account correlations in nuclear decay chains). A second program takes the output of *MCuoreZ* and applies a detector response function and incorporates other read-out features.

4.1 Monte Carlo simulation

MCuoreZ is implemented in Geant4 version 4.9.6.p03. α, β, and γ particles, nuclear recoils, neutrons and muons are propagated down to keV energies, with an optimization done on the different volumes to balance simulation accuracy and speed. We have chosen the Livermore physics list, and particles can be generated and propagated in the bulk and on the surface of all components. The surface contamination is modeled, according to diffusion processes, with an exponential density profile and a variable depth parameter.

Single radioactive decays as well as the ^{238}U and ^{232}Th decay chains have been implemented using the G4RadioactiveDecay database. $2\nu\beta\beta$ is parameterized according to [25]. The generation of external muons, neutrons and γ is described in [18,19].

Due to the low counting statistics in CUORE-0 data some components are indistiguishable (i.e. exhibit degenerate spectral shapes)[1] and can be grouped, provided that the prior on their material contamination is properly evaluated. This simplification reduces the number of free parameters in the final fit of the simulation to the data. A similar case holds for components made of the same material (i.e., characterized by an identical contamination): their simulations can be grouped once scaled by mass or surface to properly equalize the contamination densities.

The detector as built and the geometry as implemented in *MCuoreZ* are shown in Fig. 1. The outermost volume included in CUORE-0 geometry is the external neutron shield. Although its contamination is negligible, its effect on the propagation of external neutrons and muons is important.

The next layer is the external lead shield made of modern lead (*ExtPb*). Only the inner 10 cm are simulated, since self-shielding is so high that the contribution from the outer volume is negligible.

The cryostat is then modeled as composed of two volumes: the Cryostat External Shields (*CryoExt*) and the Cryostat Internal Shields (*CryoInt*).

The *CryoExt* groups three components made of copper that has been underground for more than 25 years. These components exhibit degenerate spectra and the only prior considered for their contamination is that on ^{60}Co derived from their identical history. Included in this volume are a small amount of superinsulation material (Mylar and Al) and the gap between the OVC (cryostat Outer Vacuum Chamber) and the *ExtPb*. The *ExtPb* is enclosed in acrylic glass and flushed with nitrogen (anti-radon box) to prevent radon from filling this gap and entering the experimental volume.

The *CryoInt* groups three shields made of the same newer copper, underground since 2002: the IVC (cryostat Inner Vacuum Chamber), the 600 and 50 mK shields. The roman lead [26] shield (*IntPb*) is inserted between the IVC and the 600 mK shield. The *Holder* is the structure that holds the crystals. It is made from NOSV copper, a special copper alloy from Aurubis company suitable for cryogenic use, cleaned according to the CUORE protocols [14]. It has two main parts: the frame that supports the crystals and the surround-

---

[1] Some degenerate sources could be disentangled by considering distribution of events across the detector. In order to keep the number of free parameters small and the number of simulated configurations tractable, we do not use position of the events in this analysis, and average the spectra over the entire tower.

Table 3 Elements of the CUORE-0 setup implemented in *MCuoreZ* with the values of their volumes, surface and mass. Inside the cryostat all the volumes are in vacuum but the Main Bath that is filled with LHe. In Column (5) we indicate the short-name of the component that is used in this paper. Some components are not used as source contamination in this analysis, but they exist in the simulation, including their absorption properties

Component description	Volume [dm^3]	Surface [dm^2]	Mass [kg]	Component name
External neutron shield (B+PET)	1385.2	2859.2	2770.3	
External lead shield (Pb)	2177.6	2338.9	24,694.0	*ExtPb*
OVC shield (Cu)	53.2	894.6	474.8	
Superinsulation layers (Cu + Mylar + Al)	18.3	728.0	163.2	*CryoExt*
Main bath (Cu)	16.3	692.7	145.0	
Cryostat top plate (Brass)	0.3	6.9	2.3	
Dilution unit (Fe)	0.5	4.3	3.8	
IVC shield (Cu)	5.1	278.3	45.6	
600 mK Shield (Cu)	2.2	178.7	19.8	*CryoInt*
50 mK Shield (Cu)	1.9	154.8	16.9	
Roman lead shield	17.8	198.7	202.3	*IntPb*
Detector tower box (NOSV Cu)	0.8	93.3	6.8	
Frames (NOSV Cu)	0.3	23.5	2.6	*Holder*
Wire trays (NOSV Cu)	0.1	14.4	0.6	
Junction bars (NOSV Cu)	0.1	14.4	0.6	
NTD thermistors (Ge)	4.7×10^{-4}	0.2	0.002	
Cabling tapes (Cu+PEN)	2.2×10^{-2}	5.8	0.04	*Small Parts*
Wire pads (Cu)	3.1×10^{-4}	0.6	0.003	
Crystals spacers (PTFE)	0.1	12.6	0.2	
TeO$_2$ crystals	6.5	78.0	39.0	*Crystals*

ing cylindrical box. Finally, the *Crystals* are designed as TeO$_2$ cubes with identical contaminations.

In Table 3, the components listed as *Small Parts* are not included in the following analysis because of their small mass and negligible contamination (see Tables 1, 2). Only the PTFE spacers could provide a sizable contribution to the background, however, their spectra are degenerate with the *Holder* ones, therefore their contribution is included in the latter element.

4.2 Monte Carlo data production

In order to make the Monte Carlo reproduce experimental data – as already anticipated – a second code is used to recreate the detector time and energy response. We account for the timing resolution of each crystal by combining energy depositions that occur in the same crystal within a window of ±5 ms. The absolute time of events is assigned based on a random distribution with an event rate of 1 mHz (the experimental rate during physics runs) and any physical coincidences from *MCuoreZ* are preserved.

Once the simulated events are correlated correctly in time, the resulting energy depositions are smeared with a Gaussian energy response function. The width of the function varies linearly with energy and is based on the FWHM resolution measured on γ-peaks in the $\mathcal{M}$ spectrum, between 511 and 2615 keV.

We reproduce also the energy dependence of the trigger efficiency. This is experimentally evaluated for each bolometer using heater-generated pulses with variable amplitudes. For each amplitude (then converted into a particle equivalent energy) the efficiency is defined as the number of triggered signals over the generated ones. The efficiency vs. energy curve is interpolated with an Erf function and used in simulation data production.

As is done in the experiment, events with coincidences in multiple bolometers within a ±5 ms window are combined into multiplets. Pile-up events (i.e. events occurring in the same bolometer within the pile-up rejection window set by the analysis – see Sect. 2) are removed to account for dead time.

The simulation properly reproduce the γ particle energies, since we calibrate CUORE-0 spectra using ^{232}Th γ

Fig. 2 CUORE-0 source calibration measurement. *Top panel* Comparison of $\mathcal{M}_1$ spectrum with its *MCuoreZ* simulation. Peaks are grouped in a single bin, while in the continuum the minimum bin size is 15 keV. *Bottom panel* bin-by-bin ratio between counts in the experimental spectrum and counts in the reconstructed one. We observe a less than 10% discrepancy in the rate at low energies (<300 keV) that is more likely due to small errors in the geometry reconstruction
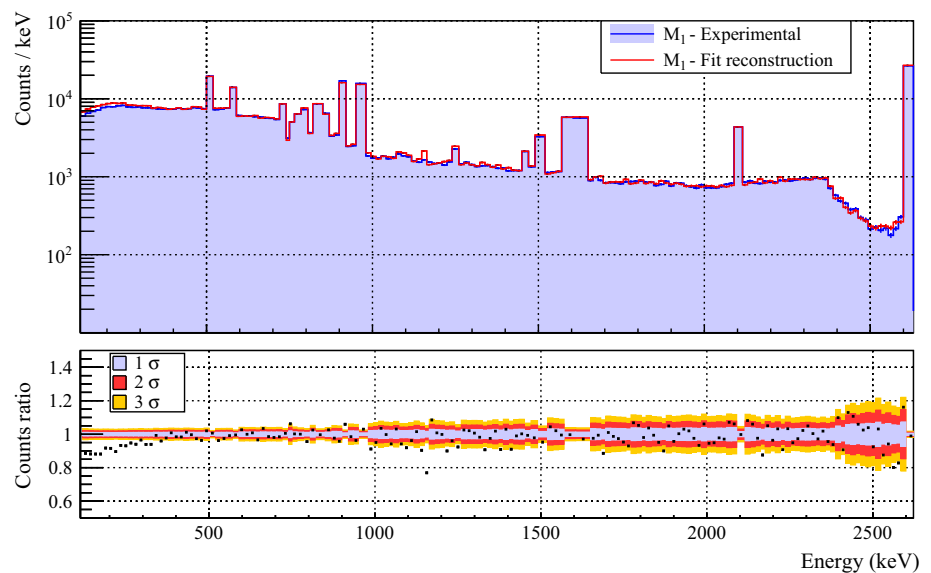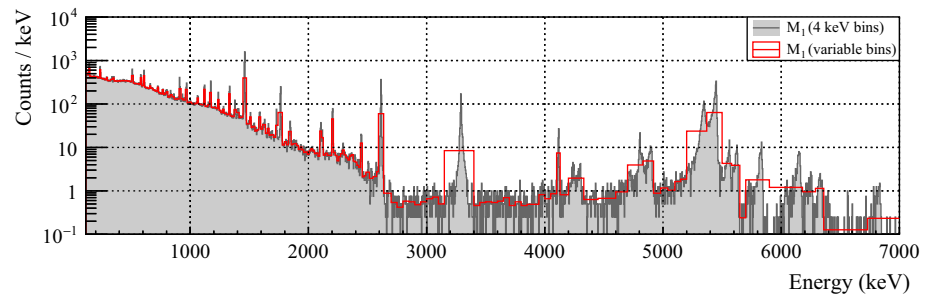

Fig. 3 CUORE-0 $\mathcal{M}_1$ spectrum with fixed 4 keV binning (*gray*) and with the variable binning used for the background model fit (*red*). The variable binning is used to reduce the effects of statistical fluctuation and/or of *line* shape (see text for more details)

lines. However, we observe in our data an energy quenching effect for α particles compared to γ, which makes the measured energies higher than the known energies [27,28]. We account for this effect in the simulations by shifting α energy depositions by 0.8%, which is the average shift observed for ^{232}Th and ^{238}U α peaks visible in CUORE-0 background spectrum.

5 Reconstruction of the calibration source

We use calibration data to test the *MCuoreZ* simulation. The thoriated wire calibration source is deployed between the *CryoExt* and the *ExtPb*, therefore its simulation involves all volumes internal to the *ExtPb*. The calibration data rate is about 100 times higher than in physics runs, so pile-up effects become sizable. Figure 2 shows that with proper treatment of pile-up effects, we achieve a good data-simulation agreement. We observe small deviations in the low-energy region between 100 and 300 keV and on a few peaks. The deviation in the low-energy region (the origin is still unknown) is a potential source of systematic errors that will be considered in Sect. 8. For what concerns peaks, the largest deviation observed is a 7% difference on the ^{228}Ac line at 1153 keV (branching ratio 0.1%). We

traced this effect to the Geant4 version[2]; anyway it has no consequences on the background reconstruction since it involves only few very low intensity lines.

6 Construction of background model

The really critical part of the background model construction is the determination a priori of the most relevant sources to be included in the fit. Omitting a relevant source could lead to a poor fit or, even worse, a good fit to the wrong model. The degeneracy of many of the sources energy spectra introduces a further complication. The analysis reported in this section uses lines in the $\mathcal{M}_1$ and Σ_2 spectra to identify the radioactive isotopes contributing to the background counting rate, their possible location and any other characteristic feature that needs to be considered in the construction of the background model.

Sources such as the external muons, neutrons, and gammas are straight-forward to model since their fluxes are well known from independent laboratory measurements. The radioactive decays are more difficult to disentangle. The loca-

---

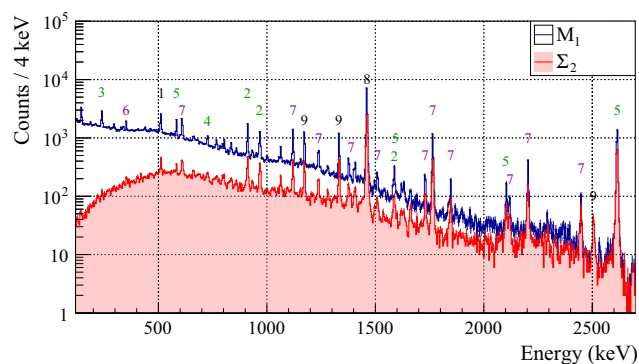[2] We recently verified that this problem is gone in Geant4 version 4.10.

Fig. 4 CUORE-0 $\mathcal{M}_1$ (*blue*) and Σ_2 (*red*) in the γ region. The peaks are labeled as follows: (*1*) e^+e^- annihilation, (*2*) ^{228}Ac, (*3*) ^{212}Pb, (*4*) ^{212}Bi, (*5*) ^{208}Tl, (*6*) ^{214}Pb, (*7*) ^{214}Bi, (*8*) ^{40}K, (*9*) ^{60}Co

tion and distribution of the contaminants must be specified, and in the case of decay chains a choice must be made between the secular equilibrium hypothesis and a break in the chain due to material handling. We use the external screening measurements presented in Sect. 3, estimates of cosmogenic exposure, and distinctive features in the data itself to select the most probable sources. These data also provide the priors for the fit.

Figure 3 shows the $\mathcal{M}_1$ spectrum. The spectrum below the 2.615 MeV γ line of ^{208}Tl includes many γ lines. Above 2.615 MeV it is dominated by α events. These are the γ and α regions respectively. The energies of the γ and α lines, the time variation of their counting rates, and the observation of prompt or delayed coincidences can all be used to select the final list of sources to be included in the fit.

6.1 CUORE-0 γ region analysis

^{232}Th and ^{238}U are natural long-lived radionuclides that generate radioactive decay chains. They can be found in almost all materials. The lines from the ^{232}Th and ^{238}U decay chains are clearly visible in Fig. 4; their intensities measured by fitting the $\mathcal{M}$ spectrum are reported in Tables 4 and 5. The lines from ^{40}K and other contaminants are also present; see Table 6.

The ^{232}Th activity is basically unchanged relative to Cuoricino, especially at high energies. This suggests that most of the observed ^{232}Th contamination is located in the cryostat and lead shields (i.e. the two structures present in both experiments). There is also a contribution from close sources, most likely the copper *Holder*, since we do not observe a large attenuation of the low-energy γ lines relative to the high-energy ones. Moreover, if the tower data are divided into floors of crystals, we do observe a floor by floor dependence that is not consistent with the one predicted by simulations. In Monte Carlo simulations this behavior can be reproduced by a point source close to the crystal that recorded the highest γ counting rate. However, the floor by

Table 4 γ lines belonging to ^{232}Th chain observed in CUORE-0 spectrum. Only lines with branching ratios above 1% are reported

Energy (keV)	Isotope	Rate (counts/kg/year)
238.6	^{212}Pb	51.0 ± 3.5
300.1	^{212}Pb	2.3 ± 1.7
328.0	^{228}Ac	6.4 ± 1.7
338.3	^{228}Ac	13.5 ± 2.1
583.2	^{208}Tl	44.0 ± 2.3
727.3	^{212}Bi	12.6 ± 1.5
795.0	^{228}Ac	8.4 ± 1.4
860.6	^{208}Tl	8.0 ± 2.3
911.3	^{228}Ac	49.2 ± 1.8
964.8	^{228}Ac	11.3 ± 1.2
969.0	^{228}Ac	29.7 ± 1.6
1588.1	^{228}Ac	14.9 ± 1.2
1620.5	^{212}Bi	2.9 ± 0.7
1630.6	^{228}Ac	3.9 ± 0.8
2614.5	^{208}Tl	80.9 ± 2.3

Table 5 γ lines belonging to ^{238}U chain observed in CUORE-0 spectrum. Only lines with branching ratios above 1% are reported. The peaks at 242 and 786 keV include a contribution from ^{224}Ra and ^{212}Bi of the ^{232}Th chain, respectively

Energy (keV)	Isotope	Rate (counts/kg/year)
242.0	^{214}Pb	6.5 ± 2.5
295.2	^{214}Pb	10.6 ± 2.3
351.9	^{214}Pb	20.9 ± 2.7
609.3	^{214}Bi	56.8 ± 2.3
768.4	^{214}Bi	7.1 ± 2.1
786.0	^{214}Pb	3.9 ± 1.4
934.1	^{214}Bi	5.6 ± 1.1
1120.3	^{214}Bi	41.4 ± 1.6
1155.2	^{214}Bi	4.4 ± 1.0
1238.1	^{214}Bi	17.4 ± 1.3
1281.0	^{214}Bi	4.9 ± 1.5
1377.7	^{214}Bi	12.3 ± 1.1
1401.5	^{214}Bi	5.7 ± 0.9
1408.0	^{214}Bi	7.9 ± 1.0
1509.2	^{214}Bi	7.5 ± 1.0
1661.3	^{214}Bi	2.9 ± 0.7
1729.6	^{214}Bi	9.3 ± 0.7
1764.5	^{214}Bi	53.5 ± 1.7
1847.4	^{214}Bi	6.5 ± 0.7
2118.5	^{214}Bi	3.8 ± 0.5
2204.2	^{214}Bi	17.0 ± 0.8
2448.0	^{214}Bi	4.4 ± 0.5

Table 6 γ lines that appear in CUORE-0 $\mathcal{M}_1$ but do not belong to ^{232}Th and ^{238}U chains

Energy (keV)	Isotope	Origin	Decay mode	Half life	Q value (keV)	Rate (counts/kg/year)
122.1	^{57}Co	Cu cosmogenic activation	EC	271.7 days	836	13.3 ± 2.1
144.8	^{125m}Te	^{125}Sb β^- decay	IT	57.4 days	145	54.8 ± 2.8
427.9	^{125}Sb	Te cosmogenic activation	β^-	2.8 years	767	6.9 ± 1.8
433.9	^{108m}Ag	Pb cosmogenic activation	EC	438 years	1922	4.6 ± 1.6
439.0	^{202}Tl	^{202}Pb EC decay	EC	12.3 days	1363	6.3 ± 1.7
600.6	^{125}Sb	Te cosmogenic activation	β^-	2.8 years	767	6.8 ± 1.4
614.3	^{108m}Ag	Pb cosmogenic activation	EC	438 years	1922	6.6 ± 1.4
661.7	^{137}Cs	Fallout	β^-	30.2 years	1176	9.8 ± 1.9
723.3	^{108m}Ag	Pb cosmogenic activation	EC	438 years	1922	6.1 ± 1.3
803.1	^{210}Po	^{210}Pb β^- decay	α	138.4 days	5408	12.8 ± 1.7
834.8	^{54}Mn	Cu cosmogenic activation	EC	312.5 days	1377	12.1 ± 2.3
1063.7	^{207}Bi	Fallout	EC	31.6 years	2398	10.9 ± 1.2
1173.2	^{60}Co	Cu cosmogenic activation	β^-	5.3 years	2824	51.8 ± 1.7
1332.5	^{60}Co	Cu cosmogenic activation	β^-	5.3 years	2824	50.8 ± 1.6
1460.7	^{40}K	Environmental	EC+β^-	1.248×10^9 years	1505	302.6 ± 3.3
1770.2	^{207}Bi	Fallout	EC	31.6 years	2398	3.6 ± 0.7

floor dependence is not seen in the α region, so the source cannot be directly facing the detectors, and is most likely located in the 50 mK copper shield. A similar anomaly was present in Cuoricino.

The two strongest γ emitters of the ^{238}U chain are the ^{222}Rn daughters: ^{214}Pb and ^{214}Bi. All of the observed ^{238}U peaks are attributed to these two isotopes. Compared to Cuoricino, the average ^{238}U activity is a factor two to three lower in CUORE-0, revealing a better cleaning of the detector components and/or a better ^{222}Rn control. Indeed, the intensity of the observed lines, particular those from ^{214}Bi, vary from dataset to dataset by as much as a factor of 3. Since ^{222}Rn is a gas, it emanates from contaminated materials in the laboratory environment and its air concentration changes depending on ventilation conditions. As described in Sect. 4, the most likely place for ^{222}Rn to enter the experimental setup is in the gap between the OVC and the *ExtPb*. Occasionally, the nitrogen flushing system inside the acrylic glass box malfunctions and the radon level increases in this volume. This additional varying component of the ^{238}U contamination is well modeled by an increase in the contamination of the *CryoExt*.

In addition, we observe a line at 803 keV due to ^{210}Po not in equilibrium with the ^{238}U chain. This is fully explained by the ^{210}Pb ($\tau_{1/2} = 22.3$ years) bulk contamination of the *ExtPb*. Before it was installed 25 years ago, this lead had a ^{210}Pb activity of 16 Bq/kg, which is now reduced by a factor ~ 2. This same line is also present in Cuoricino data. The activity reported in Table 6 for the 803 keV peak includes a contribution from a ^{214}Bi line at 806 keV from the ^{238}U chain, which cannot be disentangled.

^{40}K is a unique long-lived isotope that decays via both β^- and electron capture, with a negligible β^+ branching. The signature of this contaminant is the single γ line at 1.46 MeV, which is produced in $\sim 10\%$ of the decays. The single γ line is not sufficient to determine the activity in each volume, however, an asymmetry in the rate along the CUORE-0 tower suggests that in addition to bulk contaminants there is a ^{40}K (extended) source at the bottom of the cryostat.

A number of isotopes produced by cosmogenic activation are also identified. The most critical of these contaminants is ^{60}Co. The coincidence of its two γ lines in a single crystal produces a peak in the $0\nu\beta\beta$ ROI (at 2505.7 keV). ^{60}Co is primarily the result of fast neutron interactions on copper [29], but it can also be produced in tellurium [30,31]. Exploiting a coincident γ analysis we can set an upper limit of 3×10^{-7} Bq/kg for the ^{60}Co concentration in the crystals, i.e. well below the level needed to explain the observed rate. Therefore most of the ^{60}Co contamination is located in the copper components.

The main copper components are the *Holder*, *CryoInt*, and *CryoExt*. Following [29], we derive upper limits on their ^{60}Co activities based on the time they spent at sea-level and underground. The time spent underground before the start of data taking was a few months for the *Holder*, 14 years for the *CryoInt*, and 25 years for the *CryoExt*. Assuming the ^{60}Co to be in saturation (i.e. the condition in which the production rate equals the decay rate) in both *CryoInt* and *CryoExt* just before the underground storage, its activity today would be about 180 μBq/kg for *CryoInt* and 42 μBq/kg for *CryoExt*. These are used as upper limits for the real contamination. We have only a very rough estimate for the cosmic ray exposure

of the copper *Holder* (since this is made of many parts, each with its own history of exposure and underground storage), which results in an expected activity of $\sim 50\,\mu\text{Bq/kg}$.

As expected, we also observe ^{54}Mn and ^{57}Co from the activation of copper [32]. Due to their short half-lives, they can only be located in the *Holder*. The nuclear fallout product ^{137}Cs is also present as it was in Cuoricino, therefore it is located in the cryostat copper structures (since it cannot contaminate ancient Roman lead). Due to the low intensity of the peak *CryoInt* and *CryoExt* spectra are degenerate with each other, and we use the first to account for this contamination. The only expected contaminant due to the cosmogenic activation of the crystals themselves is ^{125}Sb and its daughter ^{125m}Te; in fact, ^{125}Sb is the only long-lived isotope produced in tellurium with high cross-section [30].

There is evidence for cosmogenic activation of the Roman lead in the *IntPb*. We observe three γs emitted by ^{108m}Ag (see Table 6), a silver isotope produced by the neutron activation of silver impurities in the Roman lead with $\tau_{1/2} = 438$ years. We observe a peak at 439 keV that is ascribed to ^{202}Tl, a daughter of the long-lived cosmogenic activation product ^{202}Pb ($\tau_{1/2} = 52.5 \times 10^3$ years). The presence of ^{202}Tl contaminant is confirmed by a gamma spectroscopy measurement of a *IntPb* sample.

Finally, we observe the two high-energy γ-peaks at 1063.7 and 1770.2 keV from the decay of ^{207}Bi without the more intense line at 569 keV, suggesting that this fallout product contaminates the *ExtPb*, as confirmed by *MCuoreZ* simulations.

6.2 CUORE-0 α region analysis

The peaks observed in the α region of CUORE-0 (Fig. 5) come from the ^{238}U and ^{232}Th decay chains and ^{190}Pt. Due to the short range of α particles and recoiling nuclei, the sources are contaminants close to or inside the bolometers:
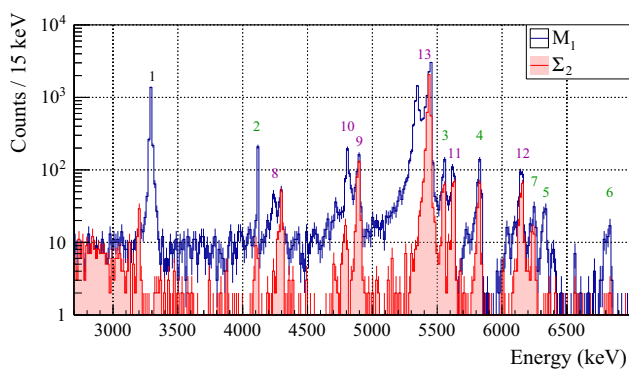
Fig. 5 CUORE-0 $\mathcal{M}_1$ (*blue*) and Σ_2 (*red*) in the α region. The energy axis is calibrated on γ. The peaks are labeled as follows: (*1*) ^{190}Pt, (*2*) ^{232}Th, (*3*) ^{228}Th, (*4*) ^{224}Ra, (*5*) ^{220}Rn, (*6*) ^{216}Po, (*7*) ^{212}Bi, (*8*) ^{238}U, (*9*) ^{234}U and ^{226}Ra, (*10*) ^{230}Th, (*11*) ^{222}Rn, (*12*) ^{218}Po, (*13*) ^{210}Po
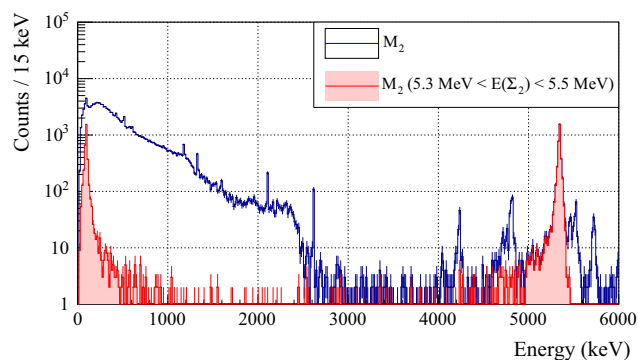
Fig. 6 CUORE-0 $\mathcal{M}_2$ spectrum (*blue histogram*, energy axis calibrated on γ). By selecting $\mathcal{M}_2$ events with a Σ_2 energy in the range 5.3–5.5 MeV, the peaks of αs and nuclear recoils due to ^{210}Pb on *Crystals* surfaces become visible (*red histogram*)

the *Holder* and the *Crystals*. The energy, multiplicity and intensity of the peaks can be used to efficiently constrain ^{238}U and ^{232}Th activities in these close components, simplifying the reconstruction of the more complicated γ region. Furthermore they allow us to differentiate bulk and surface as well as *Holder* and *Crystals* contaminations.

Contaminants in the bulk of the *Crystals* produce $\mathcal{M}_1$ events with Gaussian peaks centered at the Q-value, since the α and the nuclear recoil are detected in the same crystal.

$\mathcal{M}_2$ events are a clear indication of the presence of contaminants on the surfaces of *Crystals*; they are produced when the α or the recoiling nucleus escapes the source crystal to enter one of the neighboring ones. These events reconstruct in the Σ_2 spectrum at the decay Q-value while in the $\mathcal{M}_2$ spectra they produce two peaks each: one at the recoil energy (~ 70–100 keV) and one at the α energy (~ 70–100 keV below Q-value); see Fig. 6. As the contaminants become deeper, the α loses more energy in the material where it originates from and a low-energy tail on the α peaks (or high-energy tail on the recoil peaks) becomes more pronounced.

Contaminants on surfaces of *Crystals* also contribute to the $\mathcal{M}_1$ spectrum when both the α and the recoiling nucleus are stopped within the source crystal or the escaping particles are not detected by another bolometer.

Contaminants in the *Holder* produce $\mathcal{M}_1$ events with at most the energy of the α. Again, depending on the depth, the line shape can vary from a peak with a strong low-energy tail (shallow depth), to a flat continuum with no noticeable structures and extending far below the energy of the α (deep surface or bulk contamination).

In general, the non-ideal behavior of the detector complicates the reconstruction of α spectra. Some effects are well modeled in simulation: the energy threshold depletes $\mathcal{M}_2$ in favor of $\mathcal{M}_1$, and αs are quenched with respect to γs. Some effects are not fully understood, e.g. the broadening of all the peaks produced by surface contaminants, possibly explained

Table 7 Activities of the most prominent ^{238}U and ^{232}Th alpha peaks for both surface and bulk contaminations. Line shape is not perfectly reconstructed, therefore activities are approximate. For the ^{210}Po bulk contamination (which is decaying with ^{210}Po half-life) we report the average activity recorded during CUORE-0 measurement. A few lines are depleted by pile-up effects, therefore their activity cannot be directly measured. The energies listed in the second and third column are the nominal ones (no quenching included)

Isotope	Q-value [MeV]	α-energy [MeV]	Location Surface	Activity [10^{-2}counts/cm^2/year]
^{238}U	4.30	4.20	Crystal	1.5
^{234}U + ^{226}Ra	$\sim$4.87	$\sim$4.78	Crystal	3.6
^{230}Th	4.77	4.69	Crystal	0.6
^{222}Rn	5.59	5.49	Crystal	2.0
^{218}Po	6.12	6.00	Crystal	2.1
^{214}Po	7.83	7.69	Crystal	Pile up: β(^{214}Bi)$+\alpha$
^{210}Po	5.41	5.30	Crystal + Holder	86
^{228}Th	5.52	5.42	Crystal	1.8
^{224}Ra	5.79	5.69	Crystal	1.7
^{220}Rn + ^{216}Po	–	–	Crystal	Pile up: $\alpha + \alpha$
^{212}Bi	6.21	6.05	Crystal	1.4
^{212}Po	8.95	8.79	Crystal	Pile up: β(^{212}Bi)$+\alpha$
			Bulk	[counts/kg/year]
^{230}Th	4.77	–	Crystal	10
^{210}Po	5.41	–	Crystal	$\langle 74 \rangle$ (time average)
^{232}Th	4.08	–	Crystal	6.0

by a different response of the bolometer to surface and bulk energy depositions. We choose a variable range binning to minimize these uncertainties as described in Sect. 7.

Table 7 lists the isotopes producing the most prominent α peaks identified in CUORE-0 spectra.

Surface contaminants in the *Crystals* are identified on the basis of the Σ_2 spectrum in Fig. 5. All the visible peaks belong to the ^{232}Th or ^{238}U chains. We observe breaks in secular equilibrium, particularly evident in the case of the 5.4 MeV peak. This line, due to ^{210}Po ($\tau_{1/2} = 138$ days), is stable in time indicating an excess of ^{210}Pb ($\tau_{1/2} = 22.3$ years).

The $\mathcal{M}_1$ peaks are for the most part due to the same surface contaminations of *Crystals* with four exceptions, discussed below.

The activity of the 5.4 MeV line in the $\mathcal{M}_1$ spectrum decreases with a time scale consistent with the ^{210}Po half-life, indicating that there is a ^{210}Po bulk contamination of the *Crystals*. From this fit the average activity during CUORE-0 exposure is 2.36 μBq/kg. This violation of the secular equilibrium of the ^{238}U chain is quite common in TeO$_2$ [22] due to the chemical similarities of tellurium and polonium.

^{232}Th and ^{230}Th (a ^{238}U chain product) produce sharp lines that can be explained by a bulk contamination of the *Crystals*. Most likely, these two long-lived isotopes are the only survivors of a ^{232}Th and ^{238}U contamination in the materials used for crystal production due to chemical affinity of thorium and oxygen.

Finally, we find evidence for a bulk ^{190}Pt contamination of *Crystals*. The line in the CUORE-0 spectrum is shifted

$\simeq$15 keV above the isotope Q-value of 3249 keV, a much higher shift than the one observed for all the other lines in the α region. The crystals are grown in a platinum crucible. This contamination can be introduced during the crystal growth as a small grain of platinum locally modifying the detector response.

6.3 Source list

A list of the 57 sources used for the present analysis is shown in Table 8. The components in the first column are the 6 defined in the fifth column of Table 3. The priors in the fourth column derive mainly from Table 1. The priors for the ^{60}Co activities are discussed in Sect. 6.1. There are two components included in the analysis but not included in Table 3. One is the *50 mK Spot*, a point-like source located on the internal surface of the 50 mK thermal shield facing tower floor 10 (see Fig 1). The other is the *Bottom Plate ExtPb*, a disc-like source placed on the internal bottom plate of the external lead shield *ExtPb*. These two sources model the ^{232}Th excess observed on the floor number 10 and the ^{40}K excess observed on bottom floors, which are discussed in Sect. 6.1. In order to properly reproduce the shape of the α peaks in $\mathcal{M}_1$ and $\mathcal{M}_2$ spectra, *Crystals* and *Holder* surface contamination with a few representative depths are included in the analysis (Fig. 7). The exact choice of contaminant depth is treated as a systematic uncertainty. This is discussed in Sect. 8.

Violations of secular equilibrium in the ^{238}U and ^{232}Th decay chains are only considered when they produce a

distinguishable signature in the spectrum. A background contribution due to muons is included in the analysis; contributions from neutrons and external γs are negligible. Muons contribute mainly through γs produced by interactions in the detector components. A prior is obtained from high multiplicity data, which is compatible with the muon flux measured by other experiments.

Table 8 List of the sources used to fit the CUORE-0 background data. The columns show (1) the name of the contaminated element, (2) the source index (j in Eq. 1), and (3) the contaminant. If not otherwise specified, ^{232}Th, ^{238}U, and ^{210}Pb refer to the whole decay chains in secular equilibrium, while the label "only" indicates that only the decay of the specified isotope is generated. For surface contaminants, the simulated depth is indicated in μm. Column (4) reports the prior used in the fit, when not specified a non-informative prior is used (see text for details). Column (5) reports the posterior with the statistical error (limits are 90% C.L.). Column (6) reports the range of systematic uncertainties (limits are 90% C.L.). In the case of crystal sources, systematic uncertainties can arise from non-uniform contaminants in the different crystals

Component	Index	Bulk sources	Prior [Bq/kg]	Posterior [Bq/kg]	Systematics [Bq/kg]
Crystals	1	^{130}Te $- 2\nu\beta\beta$		$3.43(9) \times 10^{-5}$	3.1×10^{-5}–3.7×10^{-5}
	2	^{210}Po	$2.36(11) \times 10^{-6}$	$2.39(11) \times 10^{-6}$	
	3	^{210}Pb		$1.37(19) \times 10^{-6}$	5.4×10^{-7}–2.2×10^{-6}
	4	^{232}Th (only)		$7(3) \times 10^{-8}$	$<1.2 \times 10^{-7}$
	5	^{228}Ra–^{208}Pb		$<3.5 \times 10^{-8}$	$<7.5 \times 10^{-8}$
	6	^{238}U –^{230}Th		$<7.5 \times 10^{-9}$	$<3.6 \times 10^{-8}$
	7	^{230}Th (only)		$2.8(3) \times 10^{-7}$	
	8	^{226}Ra–^{210}Pb		$<7.0 \times 10^{-9}$	$<2.2 \times 10^{-8}$
	9	^{40}K		$5.1(14) \times 10^{-6}$	$<8.2 \times 10^{-6}$
	10	^{60}Co	$<3.0 \times 10^{-7}$	$<5.1 \times 10^{-7}$	
	11	^{125}Sb		$9.6(4) \times 10^{-6}$	7.5×10^{-6}–1.2×10^{-5}
	12	^{190}Pt		$2.00(5) \times 10^{-6}$	1.6×10^{-6}–2.3×10^{-6}
Holder	13	^{232}Th	$<2.0 \times 10^{-6}$	$<2.1 \times 10^{-6}$	
	14	^{238}U	$<6.5 \times 10^{-5}$	$< 1.2 \times 10^{-5}$	$<2.2 \times 10^{-5}$
	15	^{40}K	$7(2) \times 10^{-4}$	$8(2) \times 10^{-4}$	
	16	^{60}Co	$5(1) \times 10^{-5}$	$3.5(8) \times 10^{-5}$	
	17	^{54}Mn		$1.0(2) \times 10^{-5}$	$<1.7 \times 10^{-5}$
	18	^{57}Co		$2.9(3) \times 10^{-5}$	2.3×10^{-5}–3.7×10^{-5}
CryoInt	19	^{232}Th		$<1.5 \times 10^{-5}$	$<3.5 \times 10^{-5}$
	20	^{238}U		$<1.5 \times 10^{-5}$	$<3.9 \times 10^{-5}$
	21	^{40}K		$1.1(3) \times 10^{-3}$	
	22	^{60}Co	$<1.8 \times 10^{-4}$	$2.4(10) \times 10^{-5}$	
	23	^{137}Cs		$9.9(15) \times 10^{-6}$	
IntPb	24	^{232}Th	$< 4.5 \times 10^{-5}$	$5.3(7) \times 10^{-5}$	1.7×10^{-5}–6.6×10^{-5}
	25	^{238}U	$<4.6 \times 10^{-5}$	$2.7(10) \times 10^{-5}$	
	26	^{40}K	$<2.3 \times 10^{-5}$	$<2.4 \times 10^{-5}$	$<4.6 \times 10^{-4}$
	27	^{108m}Ag		$6.1(12) \times 10^{-6}$	
	28	^{202}Pb		$6(3) \times 10^{-6}$	
CryoExt	29	^{232}Th		$<1.2 \times 10^{-4}$	$<1.8 \times 10^{-4}$
	30	^{238}U		$2.4(6) \times 10^{-4}$	$<5.9 \times 10^{-4}$
	31	^{40}K		$<1.6 \times 10^{-3}$	$<2.6 \times 10^{-3}$
	32	^{60}Co	$<4.2 \times 10^{-5}$	$2.5(9) \times 10^{-5}$	
ExtPb	33	^{232}Th	$<2.6 \times 10^{-4}$	$3.1(3) \times 10^{-4}$	2.1×10^{-4}–3.5×10^{-4}
	34	^{238}U	$<7.0 \times 10^{-4}$	$5.0(6) \times 10^{-4}$	3.5×10^{-4}–6.2×10^{-4}
	35	^{40}K	$<5.4 \times 10^{-3}$	$3.1(5) \times 10^{-3}$	
	36	^{207}Bi		$5.9(5) \times 10^{-5}$	4.7×10^{-5}–7.2×10^{-5}
	37	^{210}Pb		$5.96(11)$	5.4–6.3

Table 8 continued

Component		Surface sources	Prior [Bq/cm^2]	Posterior [Bq/cm^2]	Systematics [Bq/cm^2]
Crystals	38	^{232}Th (only) $-$ 0.01 μm		$3.0(10) \times 10^{-10}$	
	39	^{228}Ra–^{208}Pb $-$ 0.01 μm		$2.32(12) \times 10^{-9}$	2.1×10^{-9}–2.7×10^{-9}
	40	^{238}U $-^{230}$Th $-$ 0.01 μm		$2.07(11) \times 10^{-9}$	1.8×10^{-9}–2.2×10^{-9}
	41	^{230}Th (only) $-$ 0.01 μm		$1.15(14) \times 10^{-9}$	
	42	^{226}Ra $- ^{210}$Pb $-$ 0.01 μm		$3.14(10) \times 10^{-9}$	2.9×10^{-9}–3.5×10^{-9}
	43	^{210}Pb $-$ 0.001 μm		$6.02(8) \times 10^{-8}$	4.8×10^{-8}–7.2×10^{-8}
	44	^{210}Pb $-$ 1 μm		$8.6(8) \times 10^{-9}$	7.2×10^{-9}–1.1×10^{-8}
	45	^{210}Pb $-$ 10 μm		$<2.7 \times 10^{-9}$	$<4.9 \times 10^{-9}$
	46	^{232}Th $-$ 10 μm		$7.8(14) \times 10^{-10}$	
	47	^{238}U $-$ 10 μm		$<3.3 \times 10^{-11}$	$<1.2 \times 10^{-10}$
Holder	48	^{210}Pb $-$ 0.01 μm		$2.9(4) \times 10^{-8}$	2.1×10^{-8}–4.3×10^{-8}
	49	^{210}Pb $-$ 0.1 μm		$4.3(5) \times 10^{-8}$	3.1×10^{-8}–5.1×10^{-8}
	50	^{210}Pb $-$ 10 μm		$<1.9 \times 10^{-8}$	$<3.9 \times 10^{-8}$
	51	^{232}Th $-$ 10 μm		$5.0(17) \times 10^{-9}$	$<1.0 \times 10^{-8}$
	52	^{238}U $-$ 10 μm		$1.39(16) \times 10^{-8}$	8.4×10^{-9}–1.6×10^{-8}
CryoInt	53	^{210}Pb $-$ 0.01 μm		$1.4(7) \times 10^{-5}$	$<2.7 \times 10^{-5}$
IntPb	54	^{210}Pb $-$ 0.01 μm		$5.1(18) \times 10^{-5}$	$<8.2 \times 10^{-5}$

Component		Other sources	Prior [Bq]	Posterior [Bq]	
50 mK Spot	55	^{232}Th	$2.4(2) \times 10^{-4}$	$2.41(18) \times 10^{-4}$	
Bottom plate ExtPb	56	^{40}K	16.8(2)	18(2)	
Muons	57		(see text)		
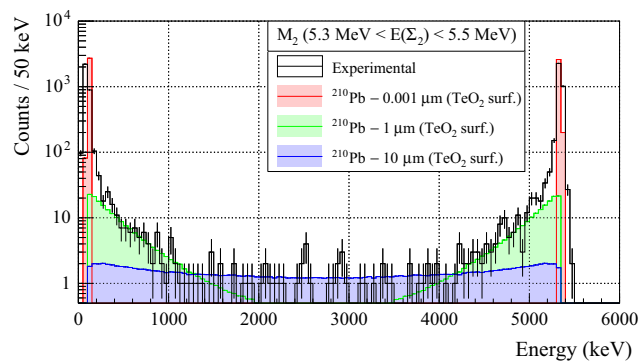
Fig. 7 Comparison between the experimental and the Monte Carlo $\mathcal{M}_2$ with Σ_2 energy equal to the Q-value of ^{210}Po α decay. The MC spectra refer to *Crystals* surface contamination with different depths parameters: 0.001, 1, and 10 μm. The normalization here is chosen to approximately reproduce the profile of the experimental data

7 Bayesian fit construction

The activities of the sources used for the background model are determined by fitting the observed $\mathcal{M}_1$, $\mathcal{M}_2$, and Σ_2 spectra with a linear combination of simulated source spectra. The expectation value of the counts in the ith bin of the experimental spectrum is given by

$$\langle C_{i,\alpha}^{\text{exp}} \rangle = \sum_{j=1}^{57} N_j \langle C_{ij,\alpha}^{\text{MC}} \rangle \qquad \alpha = \mathcal{M}_1, \mathcal{M}_2, \Sigma_2 \qquad (1)$$

where $\langle C_{ij,\alpha}^{\text{MC}} \rangle$ is the expectation value for the ith bin of the simulated spectrum for the jth source and N_j is the unknown activity of the jth source. To ensure sufficient statistics, both the experimental and the simulated spectra are summed over all the active crystals.

The fit is performed with a Bayesian approach using Just Another Gibbs Sampler (JAGS) [33–35]. JAGS exploits Markov Chain Monte Carlo simulations to sample the *joint posterior* probability distribution function (pdf) of the model parameters. Following Bayes' theorem the *posterior* pdf is evaluated combining the *likelihood* and the *prior* distributions. The available data to define the *likelihood*s are the observed counts in the bins of the experimental ($C_{i,\alpha}^{\text{exp}}$) and simulated ($C_{ij,\alpha}^{\text{MC}}$) spectra, both of which obey Poisson statistics. Therefore, the *joint posterior* pdf is

$$\text{Posterior}\big(N_j, \langle C_{ij,\alpha}^{\text{MC}} \rangle | C_{i,\alpha}^{\text{exp}}, C_{ij,\alpha}^{\text{MC}} \big)$$
$$= \prod_{i,\alpha} \text{Pois}\big(C_{i,\alpha}^{\text{exp}} | \langle C_{i,\alpha}^{\text{exp}} \rangle\big) \times \prod_{j} \text{Prior}(N_j)$$
$$\times \prod_{ij,\alpha} \text{Pois}\big(C_{ij,\alpha}^{\text{MC}} | \langle C_{ij,\alpha}^{\text{MC}} \rangle\big) \times \text{Prior}\big(\langle C_{ij,\alpha}^{\text{MC}} \rangle\big) \qquad (2)$$

Fig. 8 Comparison between the experimental $\mathcal{M}_1$ and JAGS reconstruction (*top panel*). In the *bottom panel* the bin-by-bin ratios between counts in the experimental spectrum over counts in the reconstructed one are shown; the corresponding uncertainties at 1, 2, 3 σ are shown as colored bands centered at 1. Fit residuals distribution is approximately Gaussian with $\mu = (-0.03 \pm 0.09)$ and $\sigma = (1.1 \pm 0.1)$
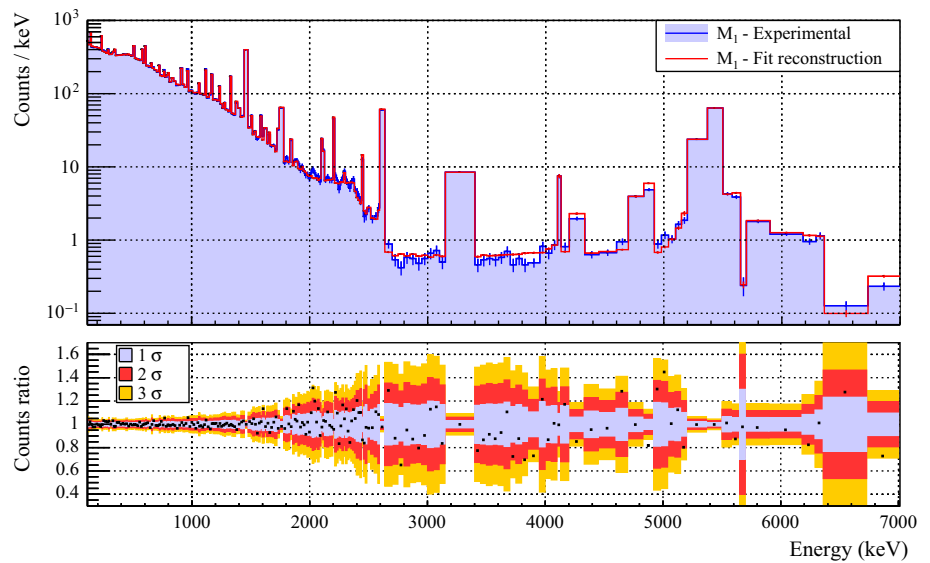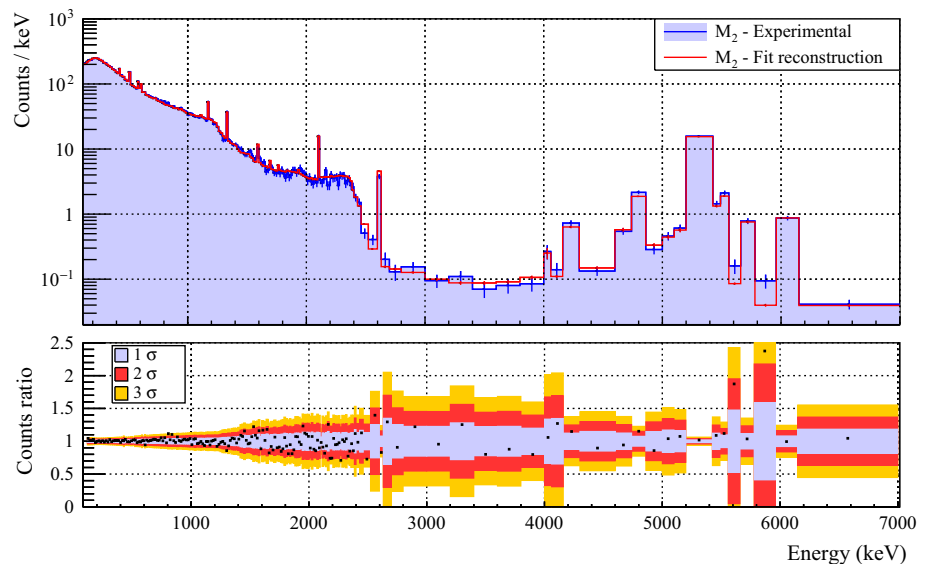

Fig. 9 Same as Fig. 8 for $\mathcal{M}_2$. Fit residuals distribution is approximately Gaussian with $\mu = (-0.13 \pm 0.08)$ and $\sigma = (1.00 \pm 0.08)$

The *prior*s for N_j, which describe our prior knowledge about source activities, are specified in Table 8. In the case of a measured activity, we adopt a Gaussian *prior* centered at the measured value with the measurement uncertainty as the width of the Gaussian. For upper limits, we adopt a half Gaussian with a width such that our 90% upper limit is the 90% value of the *prior*. In all the other cases, we use a uniform non-informative *prior* with an activity that ranges from 0 to an upper limit higher than the maximum activity compatible with the CUORE-0 data. Similarly, we use uniform *prior*s over wide ranges for $\langle C_{ij,\alpha}^{\mathrm{MC}} \rangle$.

We chose a variable binning of the spectra to maximize the information content while minimizing the effects of statistical fluctuations and detector non-ideal behavior. Therefore, to avoid systematic uncertainties due to the lineshape, all the counts belonging to the same γ or α peak are included in a

single bin. The minimum bin size in the continuum is 15 keV, and bins with less than 30 counts are merged with their immediate neighbor. The fit extends from 118 keV to 7 MeV. The threshold at 118 keV is set to exclude the low-energy noise events (contaminating few datasets) and the nuclear recoil peak (which is mis-calibrated). In building the Σ_2 spectrum, we require that the energy of each event is above threshold. An exception is set for events with $E > 2.7$ MeV in coincidence with events below the fit threshold, to correctly build-up the Q-value peaks in the α region of Σ_2 spectrum.

8 Reference fit and systematics

The *reference* fit is the result of the fit to data from the total 33.4 kg year TeO_2 exposure. The reconstructions of the experimental spectra are shown in Figs. 8, 9, and 10 for the

Fig. 10 Same as Fig.8 for Σ_2. Fit residuals distribution is approximately Gaussian with $\mu = (-0.09 \pm 0.09)$ and $\sigma = (1.0 \pm 0.1)$
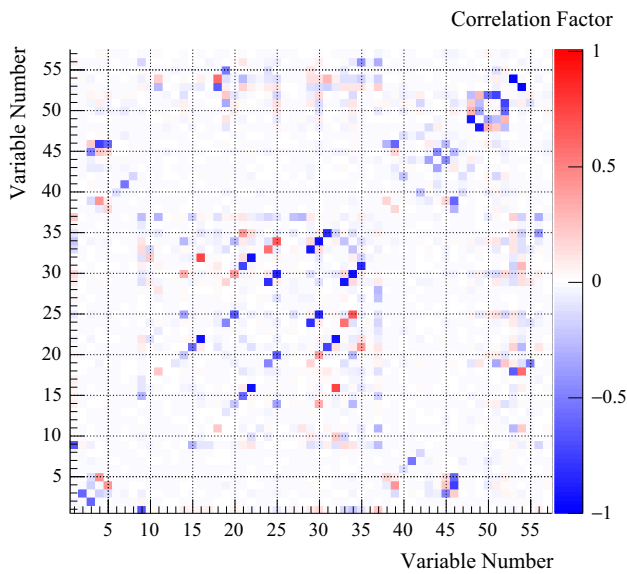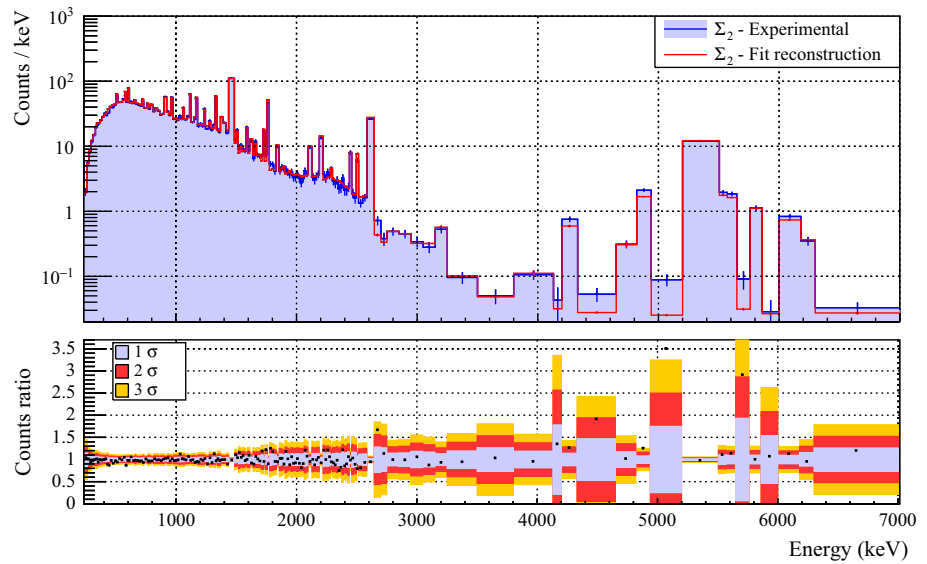

Fig. 11 Correlation matrix among the N_j parameters. The list of sources is reported in Table 8. Note the anti-correlation between the $2\nu\beta\beta$ and the ^{40}K activity in *Crystal* bulk

$\mathcal{M}_1$, $\mathcal{M}_2$, and Σ_2 spectra, respectively. The fit results for the 57 free parameters are summarized in Table 8. The marginalized posterior distributions are used to evaluate the central values and the statistical uncertainties of the activities, or to calculate 90% upper limits for undetermined contaminations.

The correlation matrix of the 57 sources is illustrated in Fig. 11. In general, most of the components used to fit the α region are not correlated to those used to reconstruct the γ region. As expected, the same contaminants in neighboring components of the experimental setup are highly correlated due to the similar spectra.

For the $\mathcal{M}_1$, $\mathcal{M}_2$, and Σ_2 spectra, the normalized fit residuals have a Gaussian-like distribution with mean 0 and stan-

dard deviation 1. The reduced chi-square with 57 parameters and 478 degrees of freedom is 1.36. We do not expect perfect statistical agreement between the data and reconstruction since the uncertainties associated with the simulated spectra account for only the statistical fluctuation in the bin counts. They do not include the systematic uncertainties in the MC simulations.

To check the stability of the background model, the dependence on priors, and the systematic uncertainties, especially those affecting the $2\nu\beta\beta$ half-life, we run a number of different fits varying the binning, energy threshold, depth of surface contaminations, priors, list of background sources, and input data.

– *Binning*: We repeat the fit with different minimum bin sizes set to 5, 10, 20, and 25 keV, and we test a uniform 15 keV binning. The latter is the only case where the reconstruction is worse, because the line shape of γ-peaks is not perfectly modeled. The $2\nu\beta\beta$ activity changes by less than 1%. These tests also cover the systematics due to miscalibration [12].

– *Fit energy threshold*: We run the fit with different energy thresholds ranging from 118 to 500 keV, covering the region where the reconstruction of the calibration source is slightly worse (Sect. 5). The quality of fit reconstruction is unchanged and the $2\nu\beta\beta$ activity variations are below 2%.

– *Contamination depth uncertainty*: We fit the α region with different depths to model surface contaminations. Several models perform similarly to the *reference* fit, however, the results of the background reconstruction, particularly the $2\nu\beta\beta$ rate, are unaffected.

– *Dependence on Prior distributions*: To evaluate the systematic uncertainty related to the *Prior* choice, we per-

form two JAGS fits. In the first fit, the half-Gaussian priors used in the case of upper limits on source activities are changed to uniform priors with the minimum at 0 and the maximum at 3σ above the upper limit. In the second fit, uniform non-informative priors are used for all components. In both cases, the global fit reconstruction is good and the $2\nu\beta\beta$ result changes by $\sim$1%.

– *Selection of background sources*: In the reference fit there are 14 undetermined sources whose activity is quoted as upper limit. To check the fit stability against the removal of these sources, we run a *minimum model* fit with only 43 sources. Once more, the global fit reconstruction and the $2\nu\beta\beta$ result are not affected.

– *Subset of data*: We compare fit results obtained with various subsets of data.

We search for time-related systematics by dividing the data into alternating datasets or grouping *Rn-low* and *Rn-high* datasets. Each study is performed with at least 1/3 of the total exposure. The *Rn-low* and *Rn-high* data are obtained by grouping the datasets in which the ^{214}Bi lines are more or less intense than the mean. This allows us to study if changes in the ^{214}Bi background influence the fit quality. The reconstruction results are compatible with the reference fit. The ^{238}U contamination in the *CryoExt*, which includes the air volume with the variable ^{222}Rn source, converges on results compatible with the different ^{222}Rn concentrations.

Finally, we investigate the dependence of the reconstruction on geometry by grouping the data by different floors: odd and even floors, upper and lower floors, the floors from 3 to 8 (central), and the complementary ones (peripherals). In this way, we explore the systematics due to model approximations. In Monte Carlo simulations we assumed contaminants to be uniformly distributed in each component of the experimental setup (except for the point sources) and we modeled the average performance of bolometers. In all studies, the reconstruction is good, but we observe variations in the activities of the sources. In particular, the $2\nu\beta\beta$ activity varies by about ±10%.

In the tests detailed above, the overall goodness of the fit remains stable, while we observe variations in the activities of the individual sources. These variations are used as an evaluation of the systematic uncertainty on the 57 source activities (Table 8, sixth column).

There are caveats using the *reference* fit results as an exact estimation of the material contamination. Indeed, degenerate source spectra allow us to use a single source to represent a group of possible sources. Examples are: the *Holder* that also accounts for the contribution of the *Small Parts*, surface contaminants in close components that are modeled with few representative depths, or bulk contamination in far components that also include surface ones.

9 ^{130}Te $2\nu\beta\beta$ decay

The background reconstruction allows us to measure the $2\nu\beta\beta$ of ^{130}Te with high accuracy. Figure 12 shows the fit result compared with the CUORE-0 $\mathcal{M}_1$. $2\nu\beta\beta$ produces $(3.27 \pm 0.08) \times 10^4$ counts, corresponding to $\sim$10% of the events in the $\mathcal{M}_1$ γ region from 118 keV to 2.7 MeV. As shown in Fig. 13, removing the $2\nu\beta\beta$ component results in a dramatically poorer fit in this region.

The $2\nu\beta\beta$ activity is $(3.43 \pm 0.09) \times 10^5$ Bq/kg, with a statistical uncertainty that is amplified by the strong anti-correlation to the ^{40}K contamination in crystal bulk (but not to other ^{40}K sources). Indeed, this is the only case where the β spectrum of ^{40}K (having a shape that resembles that of $2\nu\beta\beta$) contributes to the detector counting rate. For all the other ^{40}K sources, only the EC decay (branching ratio 89%) contributes to the detector counting rate through the 1460 keV line and its Compton tail. The *Posterior* for the $2\nu\beta\beta$ activity as obtained from the reference fit is shown in Fig 14. Also shown is the *Posterior* associated to the fit bias. This is derived from systematic studies discussed in Sect. 8 and is represented as a flat distribution. Figure 14 also shows
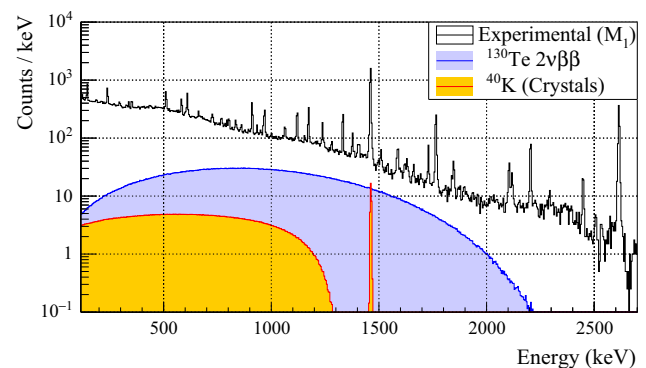

Fig. 12 CUORE-0 $\mathcal{M}_1$ compared to the $2\nu\beta\beta$ contribution predicted by the *reference* fit and the radioactive source that has the strongest correlation with $2\nu\beta\beta$, ^{40}K in Crystal bulk
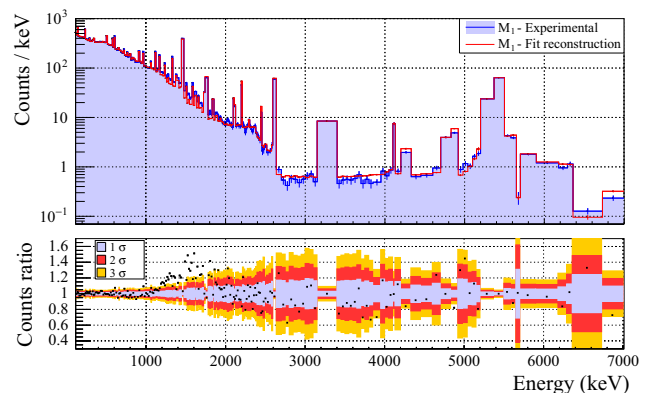

Fig. 13 CUORE-0 $\mathcal{M}_1$ compared to the reconstruction predicted by the fit without the $2\nu\beta\beta$ source
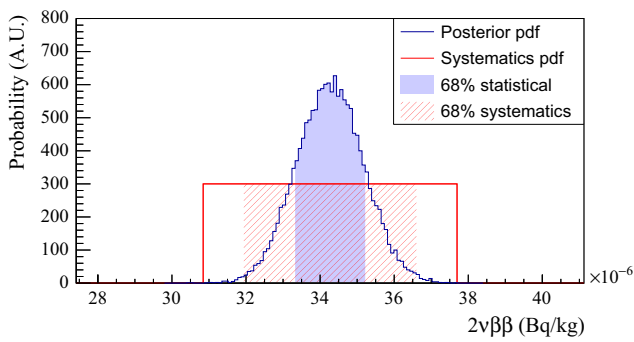
Fig. 14 *Posterior* distribution of $2\nu\beta\beta$ activity (*blue*) and systematic uncertainty range, represented as a flat distribution (*red*). The 68% confidence intervals used to quote the statistical and systematic uncertainties are highlighted by *colored areas*
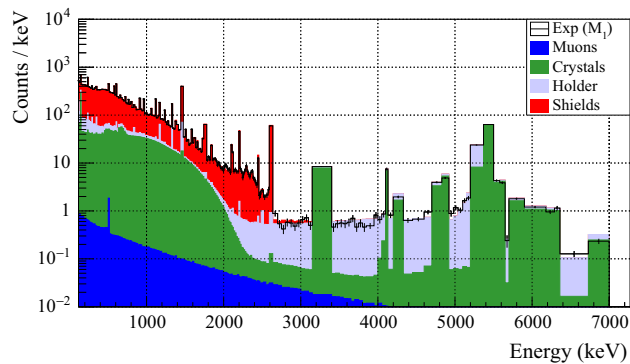

Fig. 15 Sources contributing to background reconstruction. "Shields" here stands for the sum of *CryoInt*, *CryoExt*, *IntPb*, and *ExtPb*

the 68% Confidence Intervals associated to statistical and systematic errors.

The half-life value obtained for $2\nu\beta\beta$ is

$$T_{1/2}^{2\nu} = [8.2 \pm 0.2(\text{stat.}) \pm 0.6(\text{syst.})] \times 10^{20} \text{ years}$$

10 ^{130}Te $0\nu\beta\beta$ region of interest

The signature of ^{130}Te $0\nu\beta\beta$ is a Gaussian line centered at 2528 keV, the transition energy of the isotope, in $\mathcal{M}_1$. Modeling the shape of the background in this region, especially possible subdominant peaks, and identifying the main sources of background is relevant not only for CUORE-0, but also for the future evolution of $0\nu\beta\beta$ searches with bolometers.

It is useful to group the sources used for the fit into three major classes: the two elements that will be identical (though replicated 19 times) in CUORE, *Holder* and *Crystals*, and the element that will change, i.e. the cryogenic and radioactive shield systems (the sum of the *CryoInt*, *CryoExt*, *IntPb*, and *ExtPb*). The contribution from these elements to the $0\nu\beta\beta$ region of interest (2470–2570 keV) in $\mathcal{M}_1$ are shown in Fig. 15 and listed in Table 9. The largest contribution comes

Table 9 Sources contributing to the $0\nu\beta\beta$ ROI. The flat counting rate in this region (i.e. excluding the ^{60}Co sum peak) is 0.058 ± 0.006 counts/(keV kg year) [5]. Column (2) reports the contribution of the different sources. "Shields" here stands for the sum of *CryoInt*, *CryoExt*, *IntPb*, and *ExtPb*

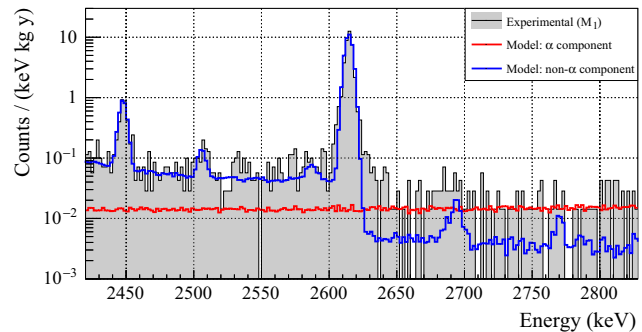| Component	Fraction [%]
Shields	74.4 ± 1.3
Holder	21.4 ± 0.7
Crystals	2.64 ± 0.14
Muons	1.51 ± 0.06

Fig. 16 Background reconstruction in the $0\nu\beta\beta$ ROI. Events due to α particles (about 24% of the ROI background) are shown in *red*. All the other events are shown in *blue*

from the shields. This is mainly ^{232}Th contamination. The *Holder* is the second largest contributor due to degraded αs from ^{238}U and ^{232}Th *deep* surface contaminants. Bulk and shallow-depth contaminants account for less than 0.3% of the background. A very small fraction of the background comes from ^{238}U, ^{232}Th, and ^{210}Pb *Crystals* surface contaminants, and from muon interactions. The systematic uncertainties are negligible.

Finally, Fig. 16 shows a wider region centered around the ROI. This plot is produced by tagging the energy depositions where at least 90% of the energy was deposited by α particles. We found ~24% of the ROI background was produced by α events. After reducing γ backgrounds from the shields, these α events are expected to dominate the ROI rate in CUORE. This motivates the development of α particle discrimination for future bolometer-based experiments; see [36] and references therein.

11 Conclusion

In this paper, we successfully reconstruct the CUORE-0 background using 57 sources modeled using a detailed Monte Carlo simulation. We find that 10% of the $\mathcal{M}_1$ counting rate in the range [118–2700] keV is unequivocally due to ^{130}Te $2\nu\beta\beta$ decay. We measure its half-life to be

$$T_{1/2}^{2\nu} = [8.2 \pm 0.2(\text{stat.}) \pm 0.6(\text{syst.})] \times 10^{20} \text{ years.}$$

Compared to previous results obtained from MiDBD [6.1 $\pm$ 1.4 (stat.) $^{+2.9}_{-3.5}$ (syst.)] $\times 10^{20}$ years [37], from Cuoricino [38], and from NEMO [7.0 $\pm$ 0.9 (stat.) $\pm$ 1.1 (syst.)] $\times 10^{20}$ years [39], this is the most precise measurement to date. We find that the background rate in the ^{130}Te $0\nu\beta\beta$ region of interest is dominated by the shields. This result gives us confidence that we are on track to achieve the requirements for CUORE.

References

1. J. Albert et al. (EXO-200 Collaboration), Nature **510**, 229 (2014)
2. A. Gando et al. (KamLAND-Zen Collaboration), Phys. Rev. Lett. **110**, 062502 (2013)
3. W.H. Furry, Phys. Rev. **56**, 1184 (1939)
4. M. Agostini et al. (GERDA Collaboration), Phys. Rev. Lett. **111**, 122503 (2013)
5. K. Alfonso et al. (CUORE Collaboration), Phys. Rev. Lett. **115**, 102502 (2015)
6. C. Arnaboldi et al. (CUORE Collaboration), Nucl. Instrum. Methods A **518**, 775 (2004)
7. R. Ardito et al. (CUORE Collaboration), (2005). arXiv:hep-ex/0501010
8. M. Redshaw et al., Phys. Rev. Lett. **102**, 212502 (2009)
9. N.D. Scielzo et al., Phys. Rev. C **80**, 025501 (2009)
10. S. Rahaman et al., Phys. Lett. B **703**(4), 412 (2011)
11. D.R. Artusa et al., Eur. Phys. J. C **74**, 2956 (2014)
12. C. Alduino et al. (CUORE Collaboration), Phys. Rev. C **93**, 045503 (2016)
13. B. Zhu, Ph. D. thesis (2016). https://cuore.lngs.infn.it/en/publications/theses
14. C. Alduino et al. (CUORE Collaboration), J. Inst. **11**(07), P07009 (2016)
15. C. Arnaboldi et al. (Cuoricino Collaboration), Phys. Rev. C **78**, 035502 (2008)
16. E. Andreotti et al. (Cuoricino Collaboration), Astropart. Phys. **34**, 822 (2011)
17. C. Bucci et al., Eur. Phys. J. A **41**, 155 (2009)
18. E. Andreotti et al. (Cuoricino Collaboration), Astropart. Phys. **34**, 18 (2010)
19. F. Bellini et al., Astropart. Phys. **33**, 169 (2010)
20. F. Alessandria et al. (CUORE Collaboration), Astropart. Phys. **45**, 13 (2013)
21. C. Arnaboldi et al., J. Cryst. Growth **312**, 2999 (2010)
22. F. Alessandria et al. (CUORE Collaboration), Astropart. Phys. **35**, 839 (2012)
23. CUORE Collaboration, LNGS Annual Report. Tech. rep. (2005). https://www.lngs.infn.it/images/REIS/Annual_Report/annual_report_2005.pdf
24. CUORE Collaboration, LNGS Annual Report. Tech. rep. (2006). https://www.lngs.infn.it/images/REIS/Annual_Report/annual_report_2006.pdf
25. J. Kotila, F. Iachello, Phys. Rev. C **85**, 034316 (2012)
26. A. Alessandrello et al., Nucl. Instrum. Methods B **142**, 163 (1998)
27. A. Alessandrello et al., Phys. Lett. B **408**, 465 (1997)
28. F. Bellini et al., J. Inst. **5**, P12005 (2010)
29. S. Cebrián et al., Astropart. Phys. **33**, 316 (2010)
30. B.S. Wang et al., Phys. Rev. C **92**, 024620 (2015)
31. A.F. Barghouty et al., Nucl. Instrum. Methods B **295**, 16 (2013)
32. M. Laubenstein, G. Heusser, Appl. Radiat. Isot. **67**, 750 (2009)
33. A. Gelman, J.B. Carlin, H.S. Stern, D.B. Rubin, *Bayesian Data Analysis*, 2nd edn. (Chapman & Hall/CRC Press, Boca Raton, 2014)
34. M. Plummer, JAGS version 3.3.0 user manual (2012)
35. D. Chiesa, E. Previtali, M. Sisti, Ann. Nucl. Energy **70**, 157 (2014)
36. G. Wang et al. (CUPID Interest Group), (2015). arXiv:1504.03599
37. C. Arnaboldi et al. (MiDBD Collaboration), Phys. Lett. B **557**, 167 (2003)
38. L. K. Kogler, Ph. D. thesis (2011). https://cuore.lngs.infn.it/en/publications/theses
39. R. Arnold et al. (NEMO-3 Collaboration), Phys. Rev. Lett. **107**, 062504 (2011)